Article

Numerical Investigation of Air-Side Heat Transfer and Pressure Drop Characteristics of a New Triangular Finned Microchannel Evaporator with Water Drainage Slits

Brice Rogie *, Wiebke Brix Markussen, Jens Honore Walther and Martin Ryhl Kærn

Department of Mechanical Engineering, Technical University of Denmark, Nils Koppels Allé, Building 403, 2800 Kongens Lyngby, Denmark; wb@mek.dtu.dk (W.B.M.); jhw@mek.dtu.dk (J.H.W.); pmak@mek.dtu.dk (M.R.K.)

* Correspondence: brogie@mek.dtu.dk; Tel.: +45 45 25 41 21

Abstract: The present study investigated a new microchannel profile design encompassing condensate drainage slits for improved moisture removal with use of triangular shaped plain fins. Heat transfer and pressure drop correlations were developed using computational fluid dynamics (CFD) and defined in terms of Colburn j-factor and Fanning f-factor. The microchannels were square 2.00×2.00 mm and placed with 4.50 mm longitudinal tube pitch. The transverse tube pitch and the triangular fin pitch were varied from 9.00 to 21.00 mm and 2.50 to 10.00 mm, respectively. Frontal velocity ranged from 1.47 to 4.40 m·s^{-1}. The chosen evaporator geometry corresponds to evaporators for industrial refrigeration systems with long frosting periods. Furthermore, the CFD simulations covered the complete thermal entrance and developed regions, and made it possible to extract virtually infinite longitudinal heat transfer and pressure drop characteristics. The developed Colburn j-factor and Fanning f-factor correlations are able to predict the numerical results with 3.41% and 3.95% deviation, respectively.

Keywords: microchannel; evaporator; water drainage; heat transfer; pressure drop; CFD

1. Introduction

Microchannel heat exchangers are attractive due to their high ratio of heat transfer area to internal volume. In recent years, they have gained increased market shares in many refrigeration and air-conditioning applications as air-cooled condensers, because of better thermo-hydraulic performance and compactness compared with traditional finned tube heat exchangers. However, their use as evaporators in refrigeration systems is challenged by (1) water condensate retention and (2) poor refrigerant distribution. The first point is extremely important in frosting conditions, since any retained water after a defrost cycle will simply freeze again on the evaporator surface.

A recent development by SAPA (now Hydro) Precision Tubing called Web-MPE offers a compromise between compactness and condensate retention, claiming a reduction of 90% water retained compared with traditional microchannel design with louvered fins [1]. The new microchannel profile designs are made with specialized drain paths in between each microchannel port, which means that the coil becomes thicker in the airflow direction.

The aim of the current work is to provide airside heat transfer and pressure drop correlations that are applicable for the design of novel ammonia microchannel evaporators for industrial refrigeration systems, e.g., cold stores, blast freezers etc., where the evaporator operates in freezing

conditions. Such ammonia evaporators are traditionally finned-tube evaporators and employ large tube diameters, large tube pitches, and large fin pitches resulting in large frosting periods (up to 24 h). The air velocity and the air throw length are high in these evaporators, hence, the tube circuitry is commonly inline to provide a low airside pressure drop. Fin types are typically limited to plain fins or wavy fins since other fin types (louver fins, offset fins) result in higher pressure drop and/or ice formation in the opening sections of the fins thus reducing their significance.

Charge minimization in ammonia refrigeration systems is pertinent due to safety restrictions associated to these systems. National authorities have implemented regulations to restrict the amount of charge in industrial refrigeration systems in many countries. Today the charge limit in Denmark is 5000 kg. Exceeding this limit leads to significant increase in cost of the plant, and installation, maintenance, and operation costs, due to increased safety precautions. It provides an incentive for academics, refrigeration engineers, and equipment manufacturers to target their research and development towards low-charge ammonia equipment, including the evaporator.

In the current paper, the backbone (airside heat transfer and pressure drop correlations) of a completely new type of low charge ammonia evaporator is developed by means of Computational Fluid Dynamics (CFD). The work is based on vertically oriented Web-MPE profiles with use of triangular plain fins. Compared to other fin geometries, such as plain fins or wavy fins, the triangular plain fins allow water to drain due to their vertical inclination. They result in less pressure drop compared with wavy fins, offset, and louvered fins. The correlations developed herein may be used by refrigeration engineers and researchers to design and optimize novel ultra-low charge ammonia evaporators. To the author's best knowledge, no previous investigations exist in the open literature considering the thermo-hydraulic characteristics of this novel microchannel design.

Computational Fluid Dynamics (CFD) has become a major tool in order to investigate the flow behavior and/or thermo-hydraulic performance inside compact heat exchangers having various fin types such as louvered fins [2–5], offset fins [6–8], wavy fins [9–11], helically wound finned-tube bundles [12,13], and plain fins [14,15]. The results of CFD simulations can be used to correlate the thermo-hydraulic performances, generally defined in terms of the Colburn j-factor and the Fanning f-factor. Chennu and Paturu [16] performed CFD simulations in order to develop air-side correlations for offset fins. They developed their correlations distinctively for laminar and turbulent regions. Ismail and Velraj [10] undertook similar work considering offset fins and wavy fins. Bacellar et al. [17] used CFD simulations to develop air-side correlations of a compact finned tube heat exchanger with staggered tube arrangement without fins. Damavandi et al. [11] expressed the air-side characteristics of a wavy fin-and-elliptical tube heat exchanger. They used neural network to express the j- and f-factors with the aim to optimize the geometry with using a j vs. f Pareto front. Deng [18] conducted CFD simulations using Large Eddy Simulations (LES) to improve correlations for flat tubes and louvered fins. Similarly, Sadeghianjahromi et al. [19] developed correlations for a finned tube heat exchanger with louvered fins, focusing on the effect of louver angle. The above references employ the effectiveness-NTU method or LMTD method with mass flow averaged temperatures to extract the j-factors. These methods incorporate the hydraulic and thermal entrance region. Other researchers assume fully developed flow and use stream-wise periodic boundary conditions, first proposed by Patankar et al. [20], for simplifying the computational domain. For example, Martinez-Espinosa et al. [21] made fully developed flow correlations for compact finned-tube heat exchangers having helically segmented finned tubes. Recent reviews on the performances of various compact heat exchanger designs can be found in Awais and Bhuiyan [22] and Qasem and Zubair [23], considering various fin types and both experimental and numerical data.

The present study investigates the new microchannel evaporator design. The objective is to establish heat transfer and pressure drop correlations in terms of Colburn j-factor and Fanning f-factor, for use in two-stream compact heat exchanger simulation and optimization codes. The correlations do not consider frosting or defrosting conditions, even though the microchannel profile has been developed herein to solve the problem of water condensate retention in evaporators during defrost. The aim of the work is rather to provide the scientific foundation that allows engineers and

researchers to design prototypes to be tested experimentally in frosting and defrosting conditions. Thus, the heat transfer and pressure drop in these conditions are subject for future work.

The paper is organized as follows: Section 2 describes the microchannel geometry, the CFD simulation design, modeling setup and verification, as well as data reduction methodology. Section 3 reports the results in terms of the correlations developed. In Section 4, the results and methodology are discussed. Finally, this is followed up by the conclusions in Section 5.

2. Method

2.1. Geometry of the Microchannel Evaporator

The microchannel evaporator is illustrated in Figure 1. It employs internal upward two-phase evaporating flow and external horizontal air crossflow. The triangular fins and drainage slits lead the water condensate downward through the evaporator during defrost.
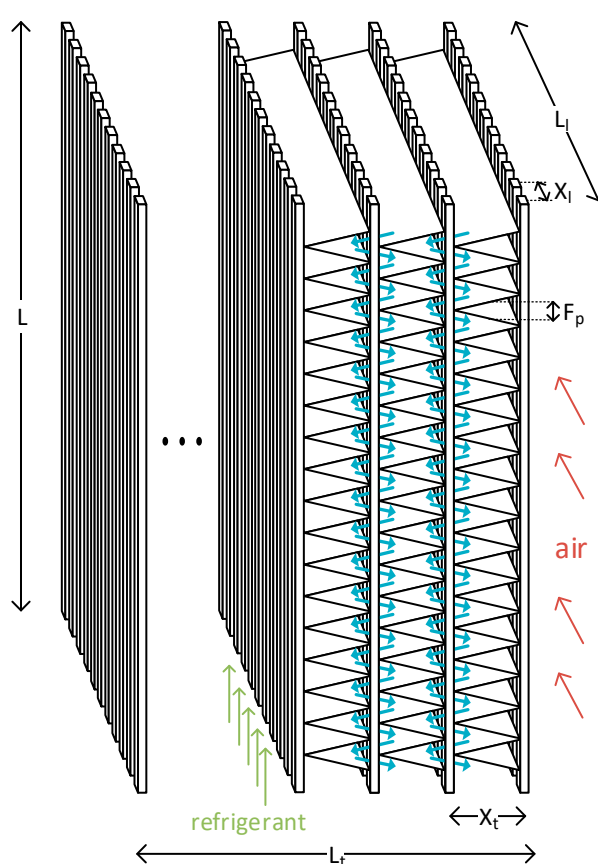
Figure 1. Sketch of the new microchannel evaporator with condensate drainage paths (blue arrows).

The microchannels were extruded and punched aluminum profiles. The extruded profiles had fixed inner and outer tube dimensions and fixed longitudinal tube pitch (Figure 2a) corresponding to the extrusion counterpart. After the extrusion process, the profiles were punched to remove a large part of the tube fins bridging the tubes in order to accommodate water drainage during defrost or dehumidifying conditions (Figure 2b). The remaining tube fins bridging the tubes were assumed to have a negligible contribution to the airside heat transfer, and thus excluded in the CFD simulations. Furthermore, the triangular plain fins had a fin thickness of 0.1625 mm.

(**a**) Side view

(**b**) Top view
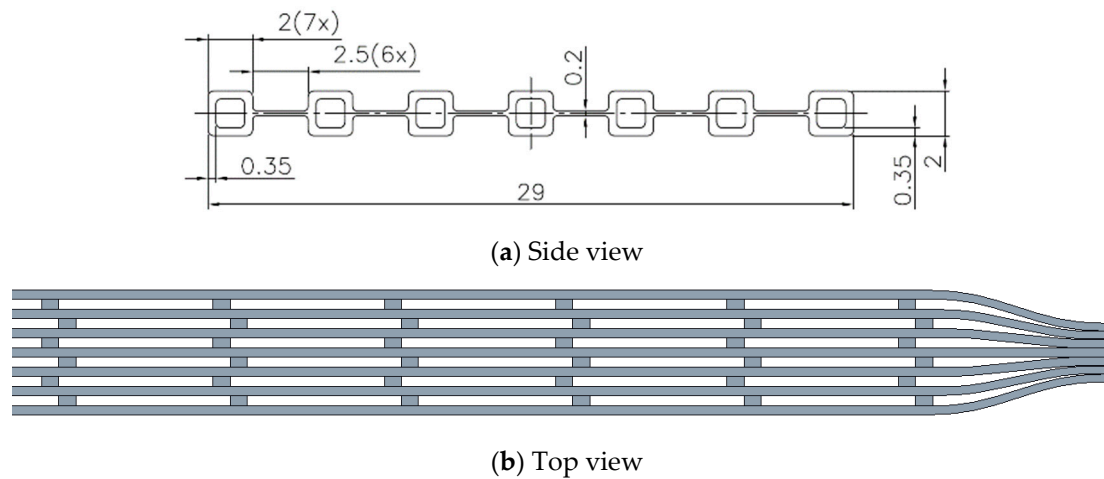
Figure 2. Extruded aluminum profile before punching (**a**) and after punching (**b**).

2.2. CFD Simulation Points

The work was based on the microchannel profile in Figure 2. This meant that the tube height/width and longitudinal pitch were fixed in the current work. With these parameters fixed, it was only the transverse tube pitch (X_t), the longitudinal length (L_l) (or the number of tube rows) and the fin pitch (F_p) that influenced the air-side heat transfer and pressure drop. A 3D model of the microchannel heat exchanger is shown in Figure 3. The fin angle (φ) was further dictated by the transverse tube pitch and fin pitch, respectively.
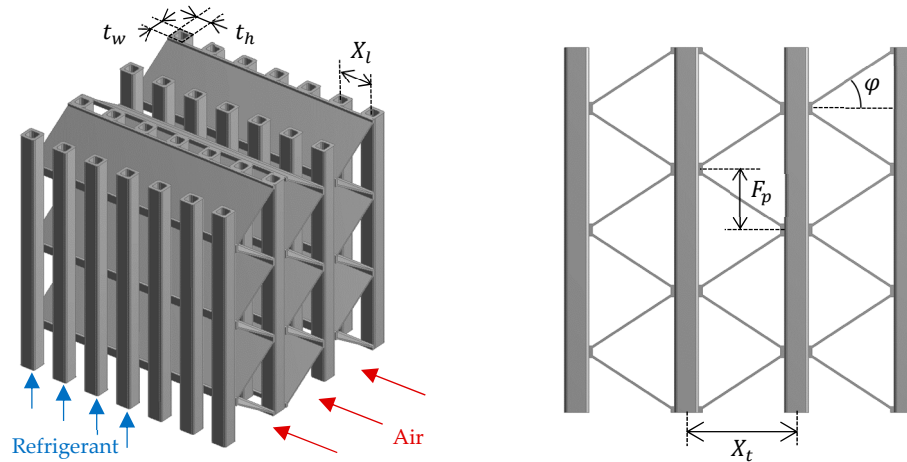

Figure 3. 3D model of the microchannel heat exchanger (seven channels, four rows).

For large fin pitches, considered in the current investigation to accommodate long frosting periods, the entrance region was found to be significant and therefore it was ensured to simulate enough longitudinal tubes (or tube rows) to establish fully developed hydraulic and thermal flow. Following this approach and to reduce the number of CFD simulations, the tube local friction and heat transfer coefficients were extracted in order to extent the global friction and heat transfer coefficients to even larger longitudinal lengths (see Section 2.4 (data reduction)). The parameterized geometry and frontal air velocity may be observed in Table 1. Some combinations of geometrical parameters were omitted (X_t = 9 mm, F_p = 7.5 mm) and (X_t = 9 mm, F_p = 10 mm) to avoid fin bending in the assembling and soldering process. The criteria used was fin angles less than 45°. In total, 42 simulations were carried out.

Table 1. Heat exchanger parameterization.

Parameters	Variation
Transverse tube pitch, X_t (mm)	9.00, 13.00, 17.00, 21.00
Fin pitch, F_p (mm)	2.50, 5.00, 7.50, 10.00
Longitudinal tube pitch, X_l (mm)	4.50
Tube rows, N_l (-)	35
Tube height, t_h (mm)	2.00
Tube width, t_w (mm)	2.00
Fin thickness, F_t (mm)	0.1625
Frontal air velocity, U_{fr} (m·s^{-1})	1.47, 2.93, 4.40

The hydraulic diameter (d_h) and the compactness ($\beta = 4\sigma/A_{tot}$) of the microchannel geometries were compared with a baseline plain finned-tube industrial refrigeration evaporator in Figure 4a and Figure 4b. The baseline is outlined in Kristófersson et al. [24,25]. The tube diameter was 15.6 mm, the tube layout was inline 50 × 50 mm, the fin thickness was 0.35 mm and the fin pitch was 12 mm, and varied from 12 to 2.5 mm to represent a comparison at a similar fin pitch.

(**a**)	(**b**)
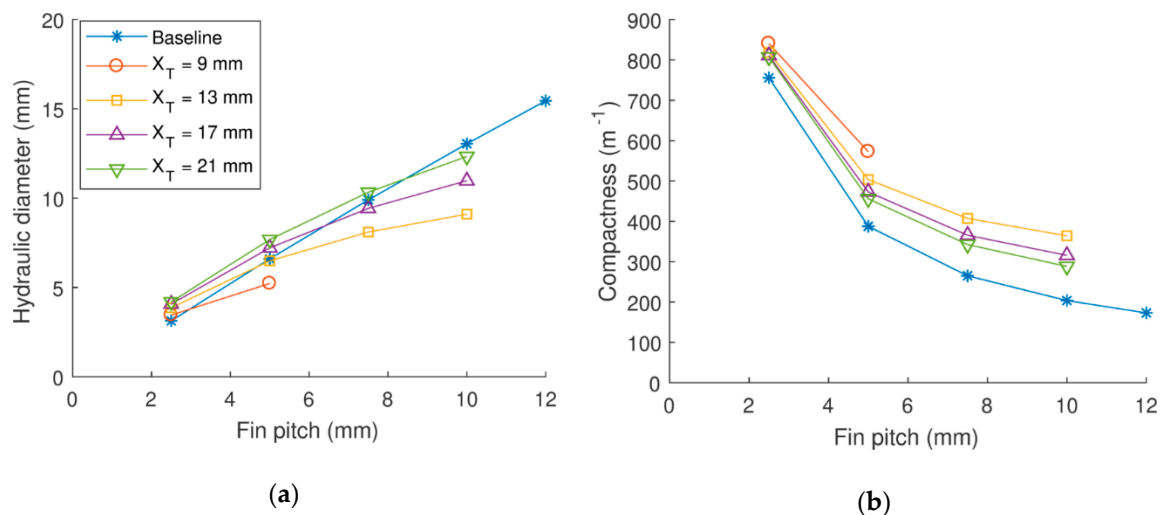
Figure 4. Hydraulic diameter (**a**) and compactness (**b**) vs. fin pitch of the microchannel evaporator geometries (Table 1) compared with the baseline finned-tube industrial refrigeration evaporator.

The hydraulic diameter of the microchannel geometries is nearly the same as the baseline finned-tube evaporator, while having more decreasing inclination as function of the fin pitch. Smaller fin pitch and transverse tube pitch result in smaller hydraulic diameters. The compactness is greater for the microchannel geometries, especially at higher fin pitch and lower transverse tube pitch compared with the baseline finned-tube evaporator. The greater differences between the hydraulic diameter and the compactness are due to the area contraction ratio (σ), which is smaller for the baseline finned-tube evaporator.

2.3. CFD Modeling Setup

CFD simulation brings an extensive knowledge of the flow behavior inside the microchannel evaporator and provides local data, which is challenging, and possibly subject to high uncertainties with an experimental setup. The CFD simulations were carried out using the commercial software ANSYS 19.1 with the CFX solver.

2.3.1. Modeling

In order to keep a reasonable simulation time, only a small part of the microchannel was modelled in the CFD simulations. Symmetries were used where the geometry allowed for it. The 3D

CFD model is shown in the Figure 5. Moreover, only a single fin was included in the computational domain.
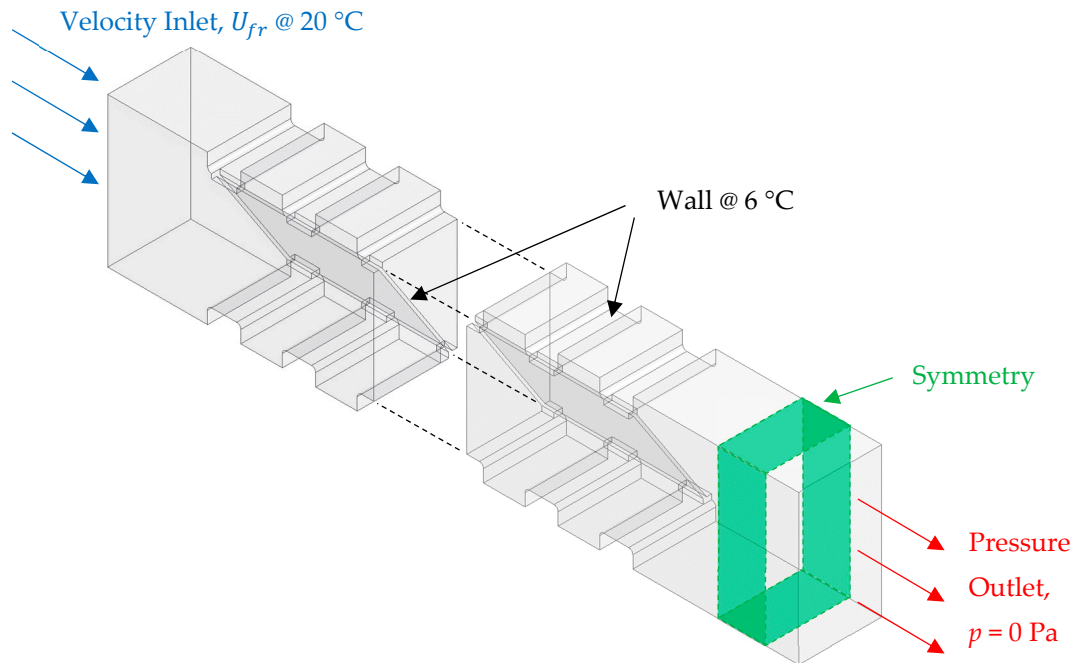
Figure 5. 3D model of the simulated geometry (X_t = 9.00 mm, F_p = 5.00 mm, N_l = 35).

The tube and fin walls were assumed to have a constant wall temperature (6 °C) consistent with the use of the effectiveness-NTU method for single stream heat exchangers, which was used to calculate the tube local and global heat transfer coefficients. Moreover, the temperature values of the wall and air inlet are independent on the heat exchanger effectiveness, which is valid as long as the air properties can be assumed constant. The derived heat transfer coefficients were, therefore, tube and fin surface averaged. The constant wall temperature means that the heat conduction through the metal (tubes and fins) was disregarded in the CFD calculations, and that it must be included when using the heat transfer correlations. In Appendix A.1, it is demonstrated that the fin efficiency for rectangular fins can be used to model the heat conduction with good accuracy, even though a heat flux concentration (2D effect) occurs near the base of the fin at the microchannel walls. Furthermore, the no-slip condition was employed at the walls, and symmetry condition at the four lateral surfaces. The air was assumed an incompressible ideal gas due to the small temperature changes.

2.3.2. Mesh Analysis

For flow around obstacles, the laminar boundary layer restarts at the tip of each tube, with a transitional flow in their wakes due to vortex formation. For inline rectangular tube configuration, the heat transfer rate is expected to be highest at the leading corner edge of each tube while decreasing along the tube longitudinally. In the wake region, recirculation zones typically appear with lower velocities and heat transfer rate. However, turbulent vortices improve the mixing and increase the heat transfer in the neighborhood regions too [26].

The restart of the boundary layer principle is similar for offset fins, which generally provide a very good heat transfer rate compared to other fin designs [23]. The transition from laminar to turbulent flow may appear for low Reynolds number, Re < 500, such as described by Sahiti et al. [27]. The range of Reynolds numbers in the current simulations is from 500 to 4000, therefore the k-ω SST turbulence model, based on the work of Menter [28], was selected. Kim et al. [29] showed that the k-ω SST turbulence model gives better performances, compared to the k-ε and realizable k-ε turbulence models, in terms of predicted *j* and *f* factors for offset fins at Re > 1000. Finally, Chimres et al. [30]

showed that the k-ω SST turbulence model results in good agreement with experimental heat transfer and pressure drop data for flow around tubes.

A mesh sensitivity analysis was performed. The y^+ was kept below one to ensure accurate resolution of the viscous boundary layer, advised by the ANSYS user guide [31] when using the k-ω SST turbulence model. The size of the computational grid was analyzed in order to ensure the grid independence. The values of the global Colburn j-factor and the Fanning f-factor are shown in Figure 6 as function of the mesh size.
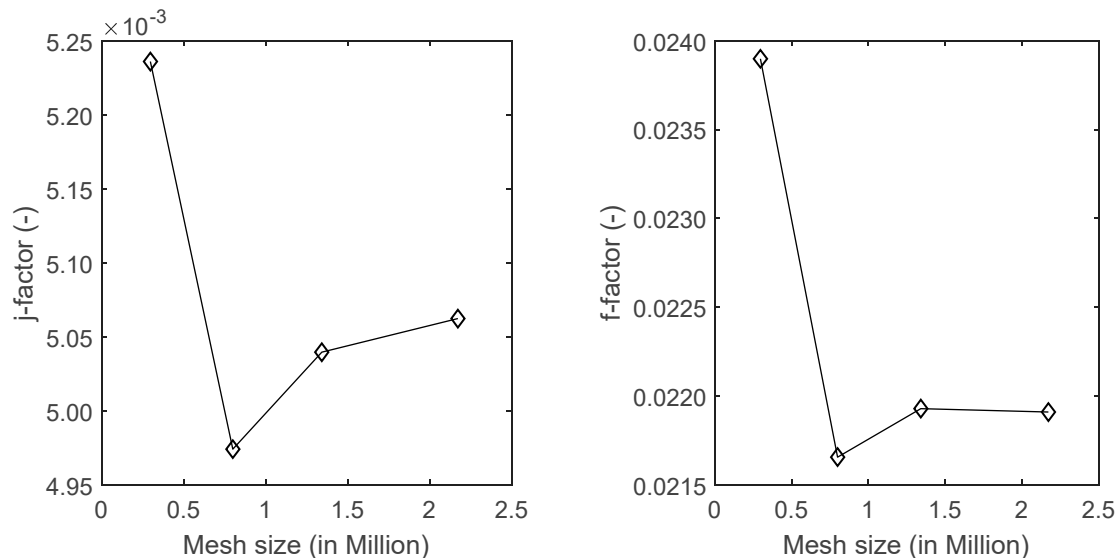
Figure 6. Colburn j-factor (left) and friction f-factor (right) as function of the mesh size (X_t = 9.00 mm, F_p = 5.00 mm, U_{fr} = 4.40 m·s⁻¹).

The difference between two consecutive values of the Colburn j-factor and the Fanning f-factor is lower than 0.5% from 1.3 to 2.2 M elements. Therefore, the mesh of 1.3 M elements was selected to have a good balance between accuracy and calculation speed. The 1.3 M mesh is shown in Figure 7.
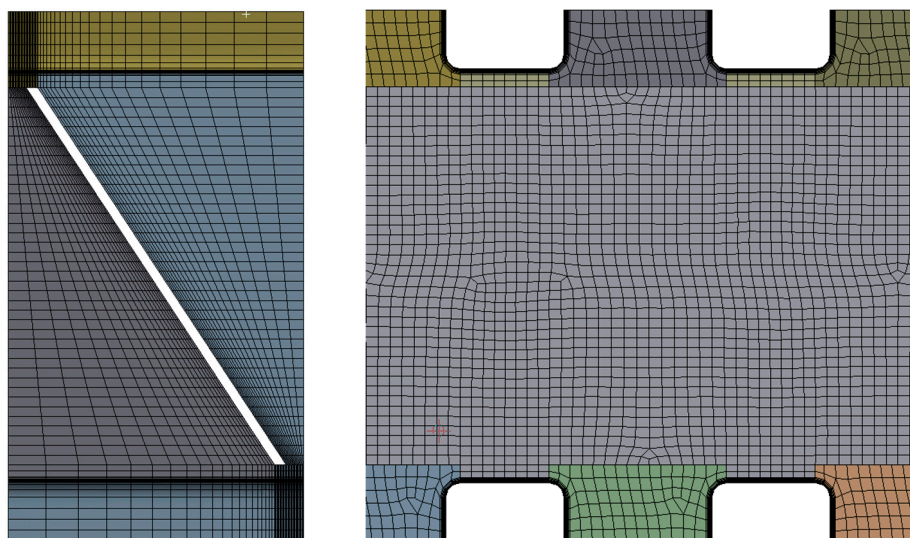
Figure 7. Computational grid. Frontal view (left) and side view (right), (X_t = 9.00 mm; F_p = 5.00 mm).

The mesh was fully structured (only hexahedral elements) to minimize numerical diffusion. Furthermore, the mesh was refined close to the wall to keep the $y^+ < 1$.
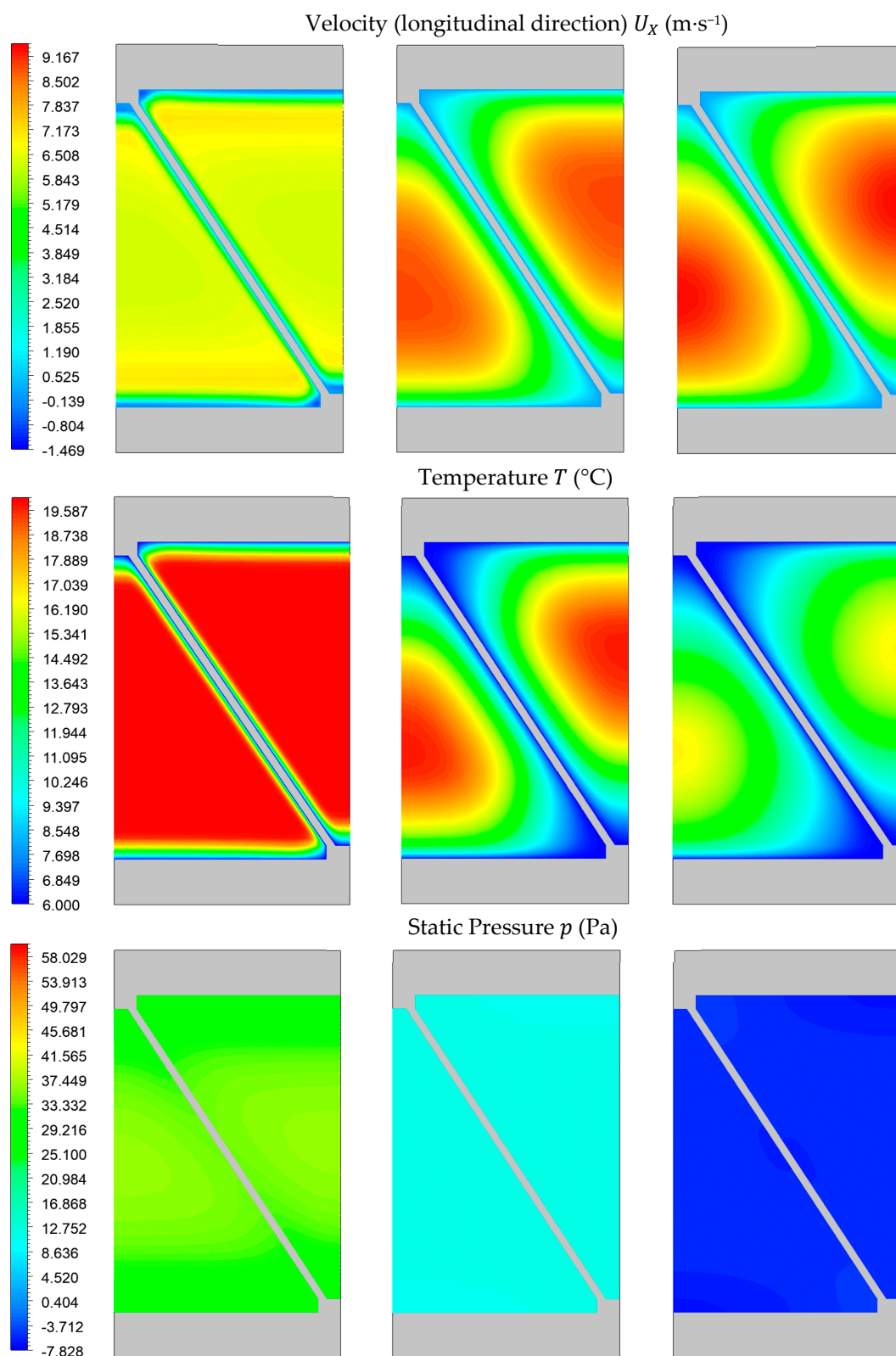
2.3.3. Velocity, Temperature, and Pressure Profiles

The longitudinal velocity, the temperature, and the static pressure contours are shown in Figure 8 and Figure 9, respectively, for the simulation: X_t = 9.00 mm, F_p = 5.00 mm, U_{fr} = 4.40 m·s⁻¹. Figure 8 shows the contours at different locations of the heat exchanger, i.e., the two first tubes (entrance region), the 17th and 18th tubes (center) and the last two tubes (exit region), respectively. Figure 9 shows the contours at different minimum cross sections normal to the airflow, i.e., the first tube (entrance region), the 17th tube (center), and the last tube (exit region), respectively.

Velocity (longitudinal direction) U_X (m·s⁻¹)

Temperature T (°C)

Static Pressure p (Pa)
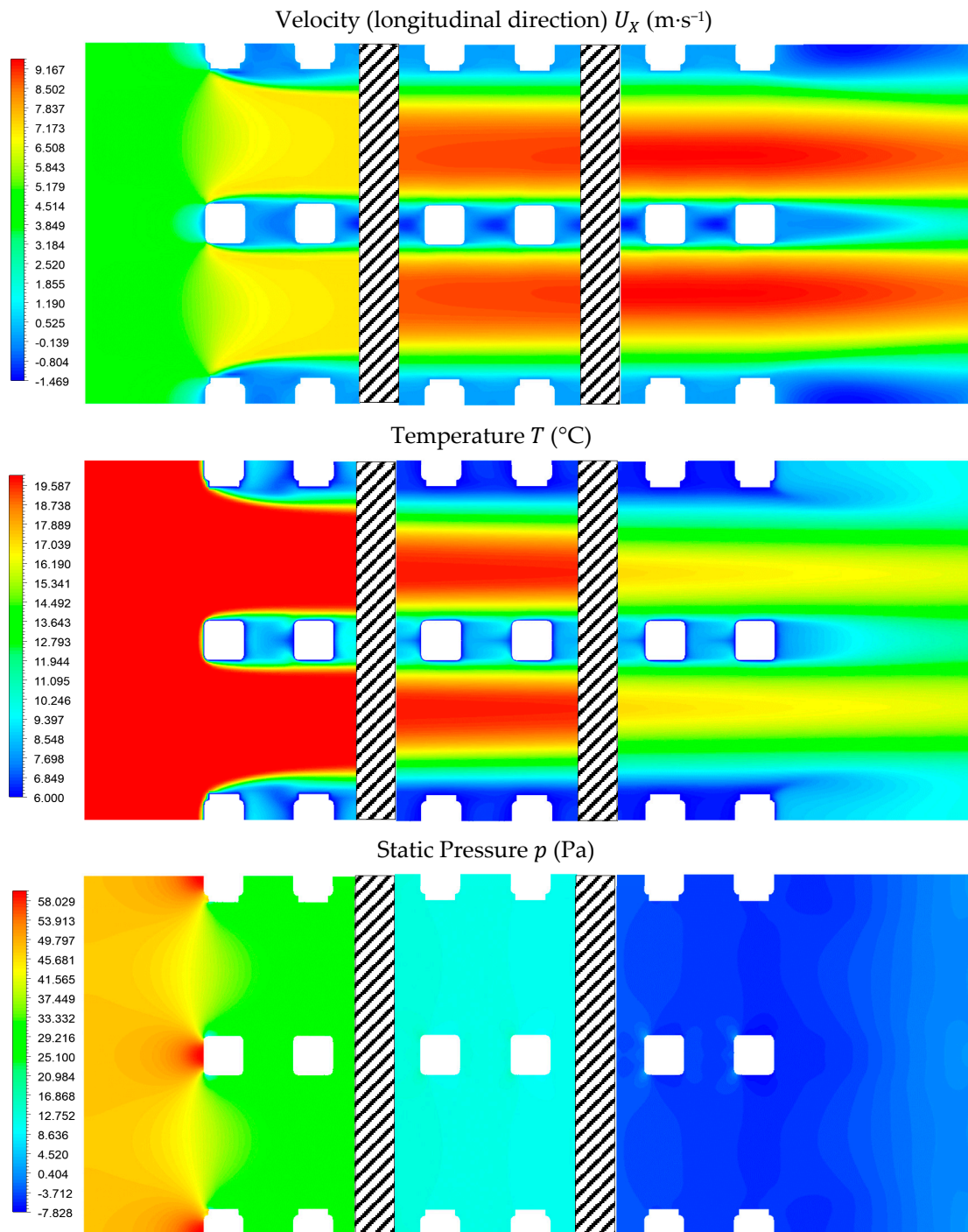
Figure 8. Longitudinal velocity, temperature, and static pressure contours at the entrance (left), middle (center), and exit (right); (side view); X_t = 9.00 mm, F_p = 5.00 mm, U_{fr} = 4.40 m·s⁻¹.

Velocity (longitudinal direction) U_X (m·s⁻¹)

Temperature T (°C)

Static Pressure p (Pa)

Figure 9. Longitudinal velocity, temperature, and static pressure contours at the entrance (left), middle (center), and exit (right); (frontal view); X_t = 9.00 mm, F_p = 5.00 mm, U_{fr} = 4.40 m·s⁻¹.

The velocity contours on Figure 8 and Figure 9 indicate that the flow develops and reaches almost fully developed velocity contour at the center region compared with the exit region. The temperature contours indicate similarity at the center and the exit region, which also confirm that the flow becomes fully developed. Additionally, the pressure change during the inlet contraction and

outlet expansion are easily observable in Figure 8. Figure 10 indicates recirculation in the wake of the channels with locally low heat transfer coefficient.
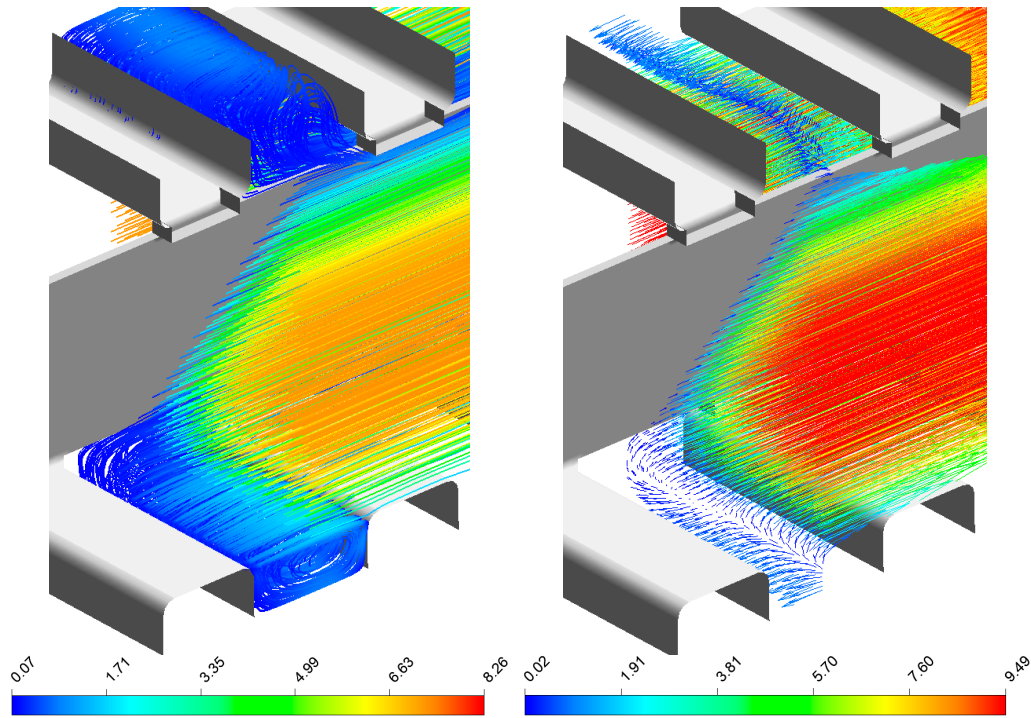
Figure 10. Velocity streamlines (left) and velocity vectors (right); X_t = 9.00 mm, F_p = 5.00 mm, U_{fr} = 4.40 m·s⁻¹.

2.4. Data Reduction

The data reduction followed simple equations to calculate the involved surface areas and flow areas etc., and matched the CFD implementation including rounding effects within 2% deviation (including the maximum core velocity, U_c). These equations, considering the computational domain, are given as follows:

$$A_{fr} = X_t \cdot F_p, \tag{1}$$

$$A_c = (X_t - t_h) \cdot F_p - \frac{P_f \cdot F_t}{2}, \tag{2}$$

$$P_f = 2 \cdot \left(\left[(X_t - t_h)^2 + F_p{}^2 \right]^{1/2} - F_t \right), \tag{3}$$

$$A_f = P_f \cdot L_l, \tag{4}$$

$$A_{tube} = \left[2 \cdot (t_w + t_h) \cdot F_p - 2 \cdot F_t \cdot t_w \right] \cdot N_l, \tag{5}$$

$$A_{tot} = A_{tube} + A_f, \tag{6}$$

where A_{fr} is the frontal area, A_c the minimum free flow area, P_f the fin perimeter, A_f the fin area, A_{tube} the bare tube area, A_{tot} the total heat transfer area. To calculate the Colburn j-factor, the effectiveness-NTU method was used with the assumption of constant wall temperature,

$$NTU_{air} = -ln\left(1 - \frac{T_o - T_i}{T_w - T_i}\right), \tag{7}$$

$$h = NTU_{air} \cdot \frac{C_{min}}{A_{tot}}, \tag{8}$$

$$j = h \cdot \frac{Pr^{\frac{2}{3}}}{\rho \cdot U_c \cdot c_p}, \tag{9}$$

where T_o, T_i, and T_w are the outlet, inlet, and wall temperature, respectively, h the heat transfer coefficient, C_{min} the minimum heat capacitance rate, Pr the Prandlt number, ρ the density, and c_p the specific heat capacity at constant pressure.

These equations were used to calculate the tube local heat transfer coefficient and global heat transfer coefficients, respectively. The tube local heat transfer coefficients were based on the mass-flow averaged inlet and outlet air temperatures of each tube row and local surface area. On the other hand, the global heat transfer coefficient was based on the mass flow averaged inlet temperature of the heat exchanger and the mass flow averaged outlet temperature of each tube row and cumulated local area.

Figure 11 illustrates the tube local and global heat transfer coefficients, and the extended global heat transfer coefficient, calculated by further integrating the fully developed tube local heat transfer coefficient:

$$h_{ext} = \frac{1}{L_{l,sim}} \cdot \int_0^{L_{l,sim}} h_{loc} \cdot dL_l + \frac{1}{L_l - L_{l,sim}} \cdot \int_{L_{l,sim}}^{L_l} h_{fd,loc} \cdot dL_l, \tag{10}$$

where $L_{l,sim}$ is the longitudinal length of the simulated geometry, h_{loc} and $h_{fd,loc}$ are the local and fully developed local heat transfer coefficient, respectively. The extended global heat transfer coefficient was integrated to provide global heat transfer coefficients for 90 tube rows in total for each of the 42 CFD simulations.
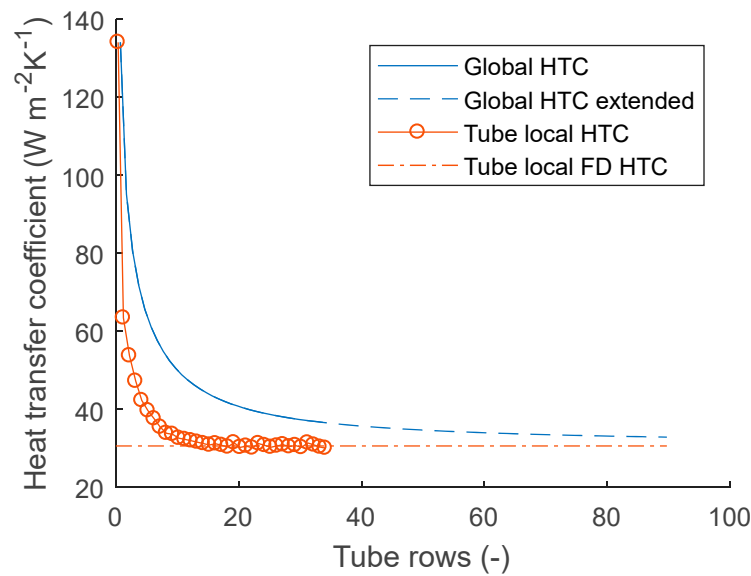
Figure 11. Extension of the global heat transfer coefficient (X_t = 13.00 mm, F_p = 7.50 mm, U_{fr} = 4.40 m·s^{-1}).

The standard deviation of the five rearmost tube rows of the simulated geometry in terms of tube local heat transfer coefficients range from 0.07 to 1.23 W·m^{-2}·K^{-1} for all the considered simulations. These values were considered reasonable for assuming thermally developed flow.

Similarly, the total pressure drop was reconstructed and extended by calculating the contraction and expansion pressure drop at the inlet (i) and the outlet (o), as well as the local core pressure drop ($core$),

$$\Delta p_{tot} = \Delta p_i + \Delta p_{core} + \Delta p_o, \tag{11}$$

$$\Delta p_i = \frac{{G_c}^2}{2 \cdot \rho_i} \cdot (1 - \sigma^2 + K_c), \tag{12}$$

$$\Delta p_o = \frac{{G_c}^2}{2 \cdot \rho_i} (1 - \sigma^2 - K_e) \cdot \frac{\rho_i}{\rho_o}, \tag{13}$$

$$\Delta p_{core} = \frac{G_c{}^2}{2 \cdot \rho_i} \cdot \left[f \cdot \frac{A_{tot}}{A_c} \cdot \frac{\rho_i}{\rho_m} + 2 \cdot \left(\frac{\rho_i}{\rho_o} - 1 \right) \right], \tag{14}$$

where Δp is the pressure drop, G_c the maximum mass velocity, σ the contraction ratio, K_c and K_e the contraction and expansion coefficient, respectively, and ρ_m the mean density. Here it was assumed that the contraction and expansion pressure drops were independent on the number of tube rows and could be directly added to the averaged local core pressure. Furthermore, the acceleration pressure drop in Equation (14) was assumed negligible. Figure 12 illustrates the simulated pressure drop, the reconstruction, and extension of the reconstruction.
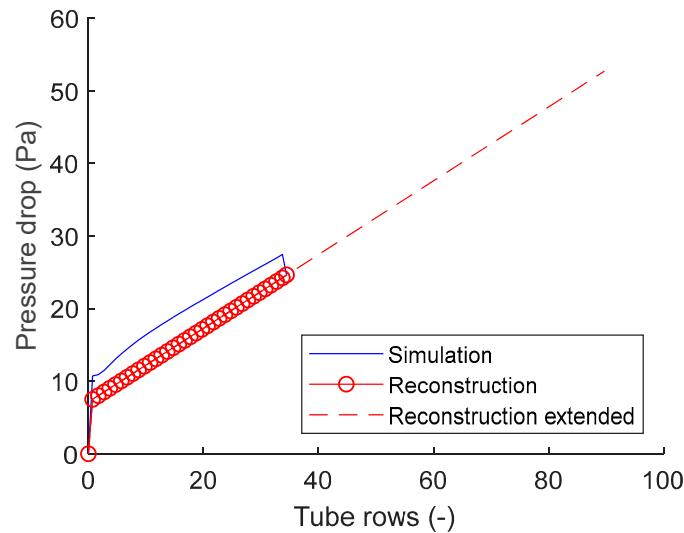
Figure 12. Reconstruction and extension of the pressure drop (X_t = 13.00 mm, F_p = 7.50 mm, U_{fr} = 4.40 m·s^{-1}).

Finally, the extended pressure drop was converted into a total friction factor, which incorporates the contraction and the expansion pressure drops, respectively, consistent with usual practice regarding compact heat exchanger pressure drop correlations. This was done by solving Equations (11)–(14) for f with $K_c = K_e = 0$ and negligible core acceleration pressure drop (term 2 in Equation (14)).

Appendix A.2 demonstrates that the extension of the global heat transfer coefficient, as well as the reconstruction and extension of the pressure drop, are indeed valid by simulating geometrical designs with 18, 35, 53, and 70 tube rows. Moreover, the results were almost identical and independent of the number of tube rows.

3. Results

3.1. Heat Transfer and Pressure Drop Regression

The reduced CFD results in terms Colburn j-factor and Fanning friction f-factor were regressed using multiple linear and nonlinear regression techniques. Moreover, the asymptotic model was used to model the transition between the entrance region (ent) and the fully developed (fd) region, respectively,

$$y^n = y_{ent}{}^n + y_{fd}{}^n, \tag{15}$$

where y denote the Colburn j-factor or Fanning f-factor, respectively. Four nondimensional parameters based on the hydraulic diameter were used to model the entrance and fully developed regions,

$$y_{ent} = b_1 \cdot Re_{d_h}{}^{b2} \cdot \left(\frac{L_l}{d_h} \right)^{b3} \cdot \left(\frac{X_t}{d_h} \right)^{b4} \cdot \left(\frac{F_p}{d_h} \right)^{b5}, \tag{16}$$

$$y_{fd} = b_6 \cdot Re_{d_h}{}^{b7} \cdot \left(\frac{X_t}{d_h}\right)^{b8} \cdot \left(\frac{F_p}{d_h}\right)^{b9}, \qquad (17)$$

where Re is the Reynolds number, $b_{1,2\ldots}$ regression coefficients, and d_h the hydraulic diameter given by,

$$d_h = \frac{4 \cdot A_c \cdot L_l}{A_{tot}}. \qquad (18)$$

Notice that the fully developed equation was independent longitudinally, in contrast to the entrance equation. The regression procedure followed the four steps:

1. Linear regression of y_{ent} based on the first five consecutive points longitudinally (the choice of five points was based on visual interpretation of the results),
2. Linear regression of y_{fd},
3. Nonlinear regression of y,
4. A repeated nonlinear regression of the coefficients b_1, b_2, b_3, b_4, b_5 and n in order to alleviate errors related to the visual interpretation in step 1.

Figure 13 illustrates the regression methodology for the j- and f-factor, respectively.

(**a**)   (**b**)
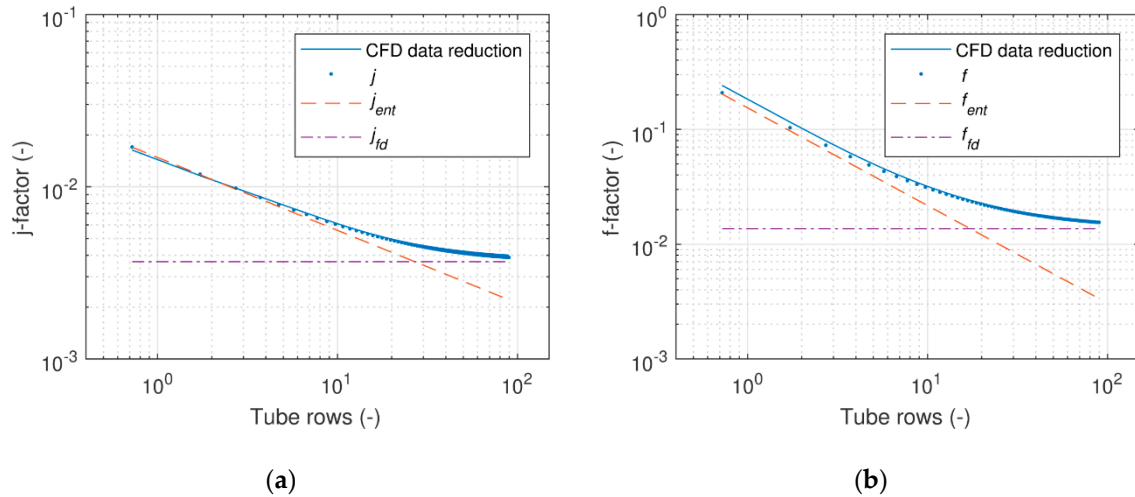
Figure 13. Regression methodology for j-factor (**a**) and friction factor (**b**). (X_t = 13.00 mm, F_p = 7.50 mm, U_{fr} = 4.40 m·s^{-1}).

Equations (15)–(17) resulted in very accurate correlations compared with the CFD simulation results. Table 2 indicates the coefficients to be used for the j- and f-factor correlations and Figure 14 shows the resulting parity plots. A total number of 42 × 90 = 3780 simulations points were used to derive the heat transfer and pressure drop correlations.

Table 2. Coefficients for the heat transfer and friction correlations.

Coefficient	j-Factor	f-Factor
b_1	0.8539	0.8665
b_2	−0.5433	−0.2804
b_3	−0.4234	−0.8512
b_4	0.0424	0.1777
b_5	−0.0966	0.9961
b_6	0.0303	1.4393
b_7	−0.2697	−0.5795
b_8	0.1015	−0.1196
b_9	0.1095	−0.2454
n	3.1784	1.2611

(**a**)

(**b**)
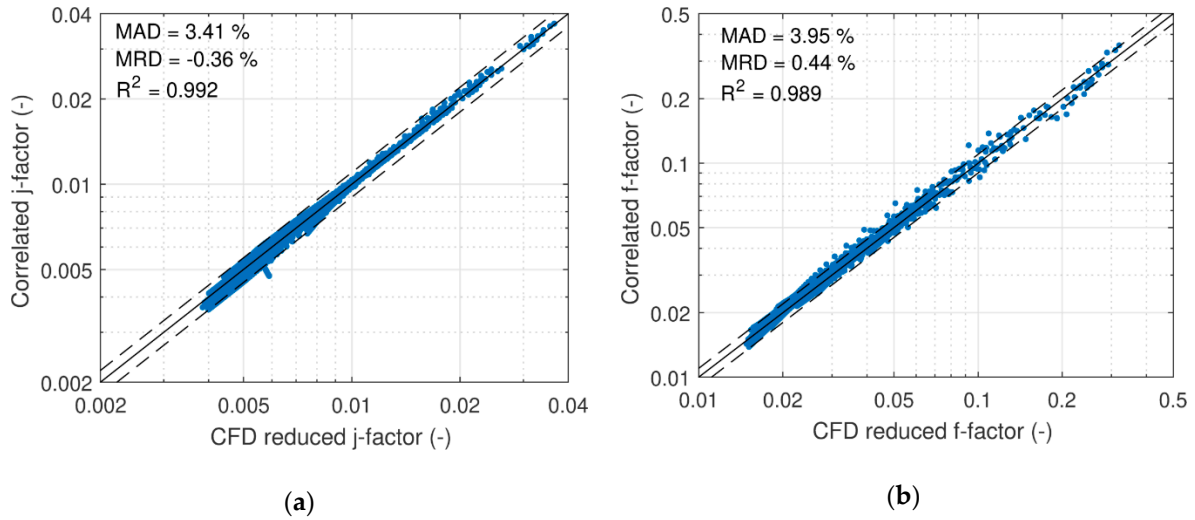
Figure 14. Parity plots for j-factor (**a**) and f-factor (**b**), dashed lines indicate 10% error.

Furthermore, the parity plots indicate the mean average deviation (MAD), mean relative deviation (MRD), and coefficient of determination (R^2). These values were computed by using the following equations:

$$MAD = \frac{1}{n} \cdot \sum_{i=1}^{n} \left| \frac{y_{i,pred} - y_{i,sim}}{y_{i,sim}} \right|, \tag{19}$$

$$MRD = \frac{1}{n} \cdot \sum_{i=1}^{n} \left(\frac{y_{i,pred} - y_{i,sim}}{y_{i,sim}} \right), \tag{20}$$

$$R^2 = 1 - \frac{\sum_{i=1}^{n}\left(y_{i,sim} - y_{i,pred}\right)^2}{\sum_{i=1}^{n}\left(y_{i,sim} - \bar{y}_{sim}\right)^2}, \tag{21}$$

where n is the number of samples, and *pred* and *sim* denote prediction and simulation, respectively. The accuracy of the correlations cannot be guaranteed when the correlations are applied beyond the ranges of the simulation points. The ranges of the simulation points were as follows:

- $d_h = 3.45 \text{ mm} - 12.33 \text{ mm}$
- $Re_{d_h} = 481 - 4084$
- $X_t/d_h = 1.4 - 5.0$
- $F_p/d_h = 0.6 - 1.1$

3.2. Analysis of Entrance Region

The results of this work indicated that the heat transfer effects of the entrance region are significant and necessary to include in the heat transfer correlation. The thermally developed region is typically claimed when the heat transfer coefficient is within 98% of the fully developed value. Figure 15 shows the number of tube rows for which this criterion is reached at different frontal velocities as a function of the hydraulic diameter, the Reynolds number, and the fin angle.

(**a**)

(**b**)

(**c**)
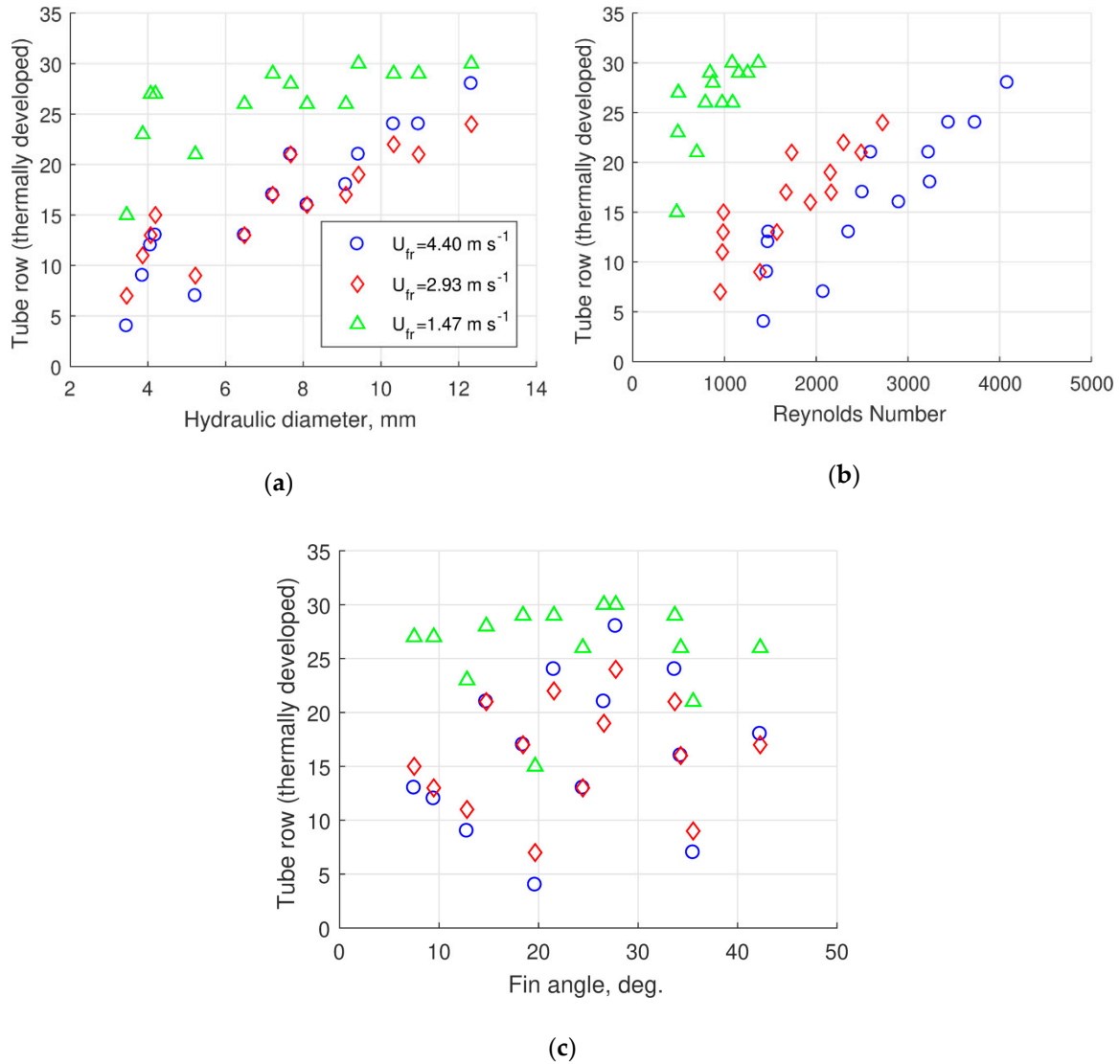
Figure 15. Number of tube rows to reach thermally developed flow at different frontal velocities vs. hydraulic diameter (**a**), Reynolds number (**b**), and fin angle (**c**).

The results show that the thermally developed flow criterion is reached at different tube rows depending on mainly the air velocity and hydraulic diameter. The highest entrance regions are found at low air velocity and high hydraulic diameter and vice versa. No particular tendencies are found with respect to fin angle.
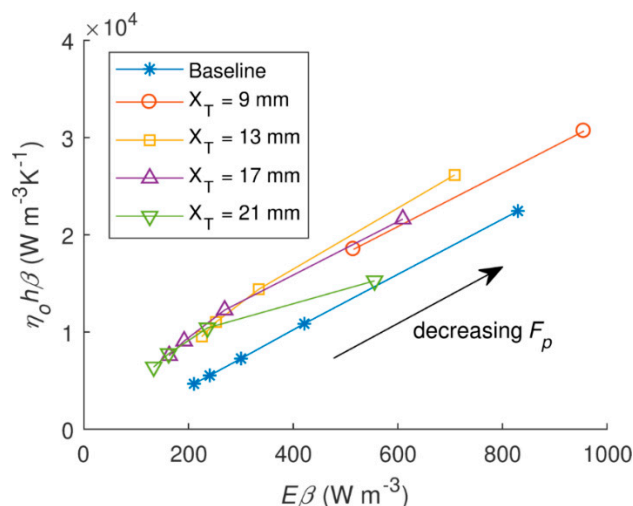
3.3. Volume Goodness Factor

The volume goodness factor, defined for extended surfaces by Shah and Sekulic [32], is used to compare the microchannel geometries with the baseline finned-tube evaporator for industrial refrigeration (see Section 2.2 for comparisons of hydraulic diameter and compactness). The volume goodness factor compares the heat transfer rate per unit temperature difference and unit core volume versus the friction power expenditure per unit core volume, both defined by:

$$\eta_o \cdot h \cdot \beta = \frac{c_p \cdot \mu}{Pr^{2/3}} \cdot \eta_o \cdot \frac{4 \cdot \sigma}{d_h^2} \cdot j \cdot Re, \tag{22}$$

$$E \cdot \beta = \frac{\mu^3}{2 \cdot \rho^2} \frac{4 \cdot \sigma}{d_h^4} \cdot f \cdot Re^3, \tag{23}$$

where η_o is the overall surface efficiency calculated using the fin efficiency for rectangular fins (see Appendix A.1), μ is the viscosity, and E is the friction power per unit surface area.

Most correlations for finned-tube evaporators in the literature are developed for staggered tube layouts as pointed out by Webb and Kim [33]. The correlations are typically developed for designs with lower fin pitch and lower number of tube rows compared with the baseline finned-tube evaporator for industrial refrigeration. This complicates the choice of correlations to compare with our results. In the following comparison, the plain finned-tube correlations by Kaminski and Groß [34] are used to calculate the j- and f- factors and the overall surface efficiency, as outlined by Fraß et al. [35]. Figure 16 shows the comparisons of the microchannel evaporator having 35 tube rows and the baseline finned-tube evaporator having eight tube rows.

Figure 16. Volume goodness factors for the microchannel evaporator geometries (Table 1) and the baseline finned-tube industrial refrigeration evaporator (U_{fr} = 2.93 m·s^{-1}, N_l = 35 and 8, respectively).

The volume goodness factors reveal that the microchannel evaporator is indeed more attractive than the baseline finned-tube evaporator, transferring more heat per unit volume at the same fluid flow power, and vice versa. In other words, the microchannel performs the best from the viewpoint of heat exchanger volume. There is however a single point (X_t = 21 mm, F_p = 2.5 mm) where the pressure drop of the microchannel evaporator increases more than the heat transfer, and results in similar performance as the baseline finned tube evaporator. This is mainly due to the low fin angle effects for this geometry. Furthermore, the variation of the number of tube rows had an insignificant effect on the volume goodness factor.

4. Discussion

The correlations obtained herein are based on (or fixed by) the microchannel profile design. For providing general correlations, the tube width, the tube height, and the longitudinal tube pitch must be parametrized too. This work did not attempt to reach beyond the actual dimensions of the extruded microchannel profile. The work must rather be viewed as a first attempt to deliver correlations for the design of such evaporators, and to be used for future research and development, especially devoted to the refrigerant charge minimization in industrial refrigeration systems. The developed correlations can be used to design the new microchannel evaporator for this purpose in dry conditions.

Frosting, defrosting, and water condensate drainage are furthermore dependent on the total size of the evaporator, especially the height as the water condensate need to travel downwards through the triangular fins. These considerations are considered for future work. A prototype evaporator is already outlined at this moment and it will be tested experimentally at the Danish Technological Institute laboratory in the near future. These tests will be used to compare the correlations accuracy.

Furthermore, tests are planned to study the cooling capacity during frost build-up and defrost performances.

Additionally, the CFD simulations should be viewed as idealized flows compared with the total evaporator flow in a real installation. There are many peculiarities in real evaporators such as airside and tube-side temperature nonuniformity, fluid flow maldistribution, nonidealized fin conduction, transitional fluid flow regimes, imperfect contact between tubes and fins, fin geometry manufacturing uncertainties, etc. These factors must be incorporated in the anticipated uncertainty during the design of the microchannel evaporator.

The correlated heat transfer coefficient is surface averaged. To be used in heat exchanger simulation codes, it should be used to calculate the fin efficiency as well. In Appendix A.1, it is demonstrated that the fin efficiency for rectangular fins can be used with good accuracy, even though a heat flux concentration (2D effect) occurs near the base of the fin at the microchannel walls.

The entrance region was found to be significant in the current analysis. Disregarding the effect of the entrance region might lead to significant underestimations of the global heat transfer coefficient, especially at lower frontal velocities where the highest entrance regions were found. It should be stressed that the current investigation considers plain triangular fins with large fin pitches. The developing region might be insignificant for other types of fins and fin pitches, e.g., because of larger secondary flows in louvered fins. No clear entrance length trends were found in terms of Reynolds number or fin angle. However, Shah and London [36] found that the entrance region reached a minimum for triangular duct flow with angles around $2\varphi \approx 55°$.

Additionally, in Appendix A.2, the extension of the global heat transfer coefficient longitudinally as well as the reconstruction and extension of the pressure drop longitudinally are assessed and discussed. Indeed, the methodology can be applied to minimize CFD simulation points and simplify the computational domain.

5. Conclusions

This paper presented heat transfer and pressure drop correlations for a new microchannel evaporator design, based on a newly developed microchannel profile with condensate drainage slits and use of triangular shaped plain fins with large fin pitch. The chosen evaporator geometry corresponds to evaporators for industrial refrigeration systems with long frosting periods. Heat transfer and pressure drop correlations were developed using computational fluid dynamics (CFD) and defined in terms of Colburn j-factor and Fanning f-factor. The computational domain covered the complete thermal entrance and developed regions, which made it possible to extract virtually infinite longitudinal heat transfer and pressure drop characteristics. Indeed, the entrance region was found to be significant compared to the typical longitudinal evaporator length. Therefore, the asymptotic model was used to correlate the entrance and developed regions, respectively. The developed Colburn j-factor and Fanning f-factor correlations were able to predict the numerical results with 3.41% and 3.95% deviation, respectively.

Appendix A

A.1 Fin efficiency

The computation of the heat transfer coefficient and fin efficiency are equally important for the design optimization of the new microchannel heat exchanger. In order to examine the fin efficiency, two heat conduction Finite Element (FEM) simulations were carried out, one with a smaller fin and another with a larger fin. Symmetry plans were used again to minimize the computational domain. The temperature of the channel internal walls was specified to 6 °C. A constant heat transfer coefficient was applied to the fin and channel external surfaces, corresponding to the thermally developed local heat transfer coefficient extracted from the CFD simulations. The contact between the channels and the fins is assumed perfect. The fin efficiency was calculated based on the results of the heat conduction simulations as follows.

$$\eta_f = \frac{\dot{Q}_{actual}}{\dot{Q}_{ideal}} = \frac{h \cdot \int_f \left(T_a - T_f\right) \cdot dA}{h \cdot A_f \cdot (T_a - T_b)}, \tag{A1}$$

where T_a is the mean fluid temperature, T_b is the fin base (or contact) temperature, and T_f is the fin temperature. The fin efficiency was compared with the analytical fin efficiency evaluated for rectangular fins

$$\eta_f = \frac{\tanh(m \cdot l_c)}{m \cdot l_c}, \tag{A2}$$

$$m = \left(\frac{2 \cdot h}{k_f \cdot F_t}\right)^{1/2}, \tag{A3}$$

with $l_c = P_f/4$. The comparison is shown in Figure A1 and the temperature contours of the heat conduction simulations are shown in Figure A2.
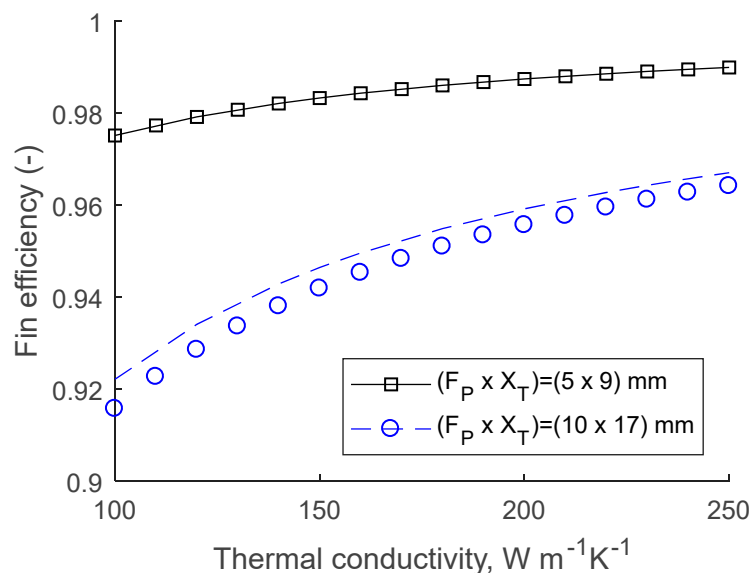
Figure A1. Fin efficiency vs. thermal conductivity for two geometries. Symbols indicate the analytical fin efficiency evaluated for rectangular fins.
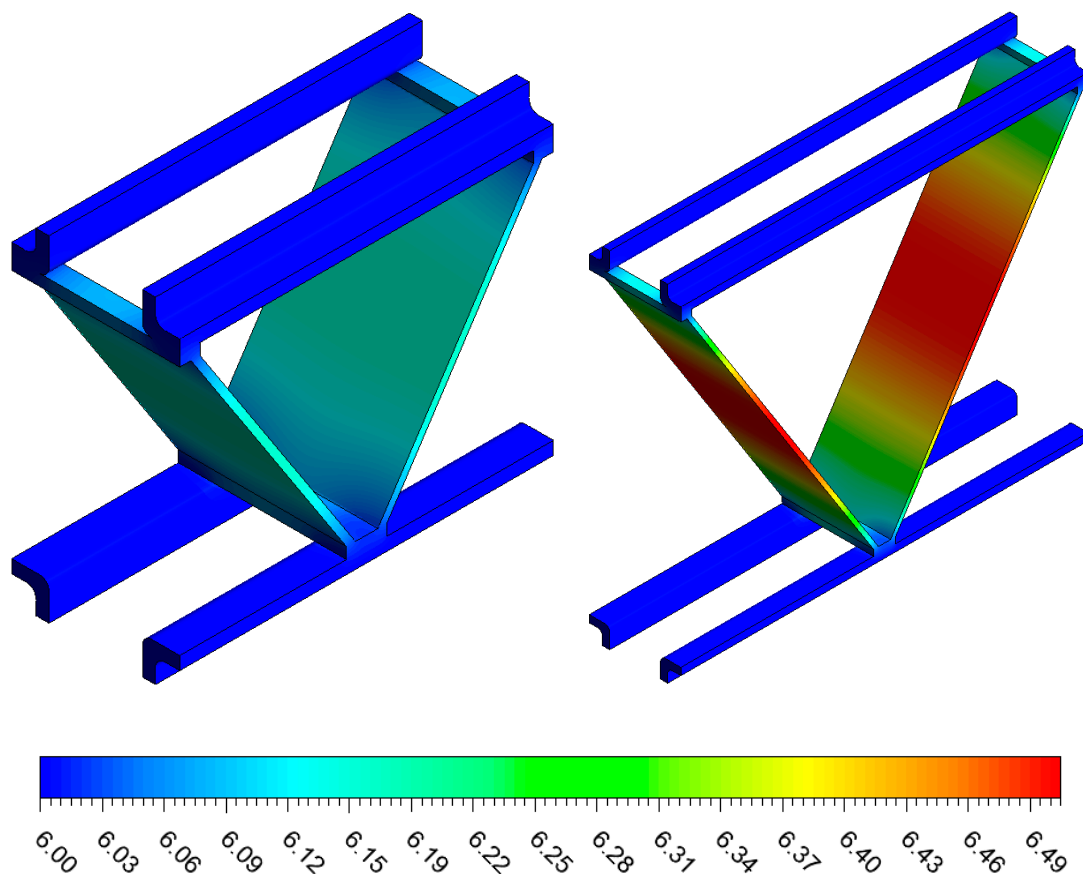
Figure A2. Temperature contours of the channel and fins. ($F_p \times X_t$ = 5.00 × 9.00 mm (left) and $F_p \times X_t$ = 10.00 × 17.00 mm (right), U_{fr} = 4.40 m·s⁻¹).

The results demonstrate that the analytical fin efficiency for rectangular fins can be used with good accuracy to model the fin efficiency of the current fin design. This holds true even though heat flux concentration (2D effects) occurs near the base of the fin at the microchannel walls.

A.2 Longitudinal Extrapolation Analysis

In this section, the validity of the extended global heat transfer coefficient is assessed. Moreover, three additional simulations were performed at different number of tube rows. The geometrically centered dimensions (F_p = 7.50 mm, X_t = 13.00 mm) and highest air velocity (U_{fr} = 4.40 m·s⁻¹) were used in these simulations. The results in terms of Colburn j-factor and the Fanning f-factor are represented in Figure A3 including the prediction of our correlation (Equation (15)).
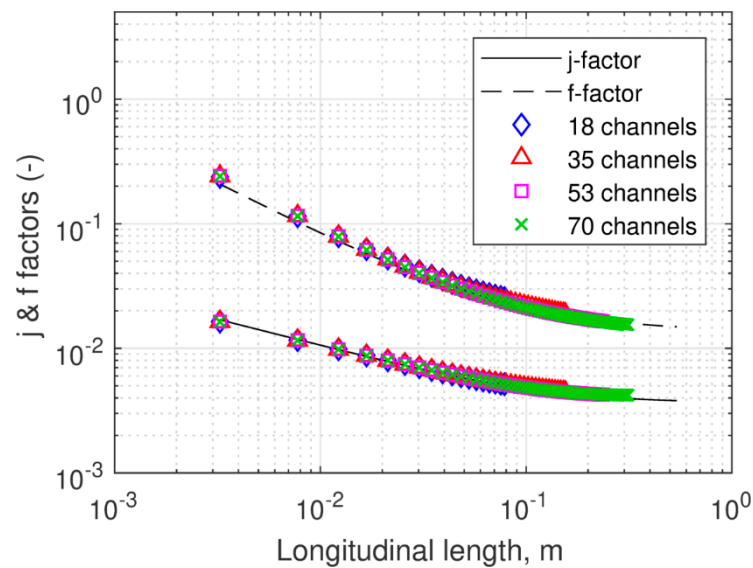
Figure A3. Colburn j-factor and Fanning f-factor vs. longitudinal length (or number of tube rows) (F_p = 7.50 mm, X_t = 13.00 mm, U_{fr} = 4.40 m·s^{-1}).

The results showed very good agreement between the results of simulations that were close to identical, and well predicted using the developed correlations. The MAE of the four simulated Colburn j-factors compared with Equation (15) were 1.9%, 1.9%, 2.4%, and 3.2% for the 18, 35, 53, and 70 tube rows, respectively. The MAE of the four simulated Fanning f-factors compared with Equation (15) were 8.2%, 3.7%, 2.2%, and 2.6% for the 18, 35, 53, and 70 tube rows, respectively. This indicated that 35 tube rows were sufficient for developing the correlations in the paper.

Nomenclature

A_c	Minimum free flow area, m²
A_f	Fin Area, m²
A_{fr}	Frontal area, m²
A_{tot}	Total heat transfer area, m²
$b_1, b_2 ... b_9$	Regression coefficients, (-)
c_p	Heat capacity at constant pressure, J kg^{-1}K^{-1}
C_{min}	Lowest heat capacity rate, W K^{-1}
d_h	Hydraulic diameter, m
E	Friction power per unit surface area W m^{-2}
f	Friction factor, (-)
F_p	Fin pitch, m
F_t	Fin thickness, m
G_c	Maximum mass velocity, kg s^{-1}m^{-2}
h	Heat transfer coefficient, W m^{-2}K^{-1}
j	Colburn factor, (-)
k_f	Thermal conductivity of fin, W m^{-1}K^{-1}
K_e, K_c	Expansion and Contraction coefficient, (-)
N_l	Tube rows, (-)
L_l	Longitudinal length, m
L_t	Transverse length, m

p	Pressure, Pa
P_f	Fin perimeter, m
Pr	Prandtl number, (-)
$\dot{Q}_{actual}$	Heat transfer to the fin, W
$\dot{Q}_{ideal}$	Heat transfer to an ideal fin, W
R^2	Coefficient of determination, (-)
Re	Reynolds number, (-)
t_h	Tube height, m
t_w	Tube width, m
T	Temperature, K
T_a	Fluid ambient temperature, K
T_b	Fin base temperature, K
T_f	Fin average temperature, K
U_c	Maximum air velocity, m s^{-1}
U_{fr}	Frontal air velocity, m s^{-1}
U_X	Flow velocity in x-direction, m s^{-1}
X_l	Longitudinal tube pitch, m
X_t	Transverse tube pitch, m
y^+	Dimensionless distance to the wall, (-)

Greek Symbols

β	Compactness, m^{-1}
η_f	Fin efficiency, (-)
η_o	Overall surface efficiency, (-)
μ	Viscosity, Pa s^{-1}
ρ	Fluid density, kg m^{-3}
σ	Contraction ratio, (-)
φ	Fin angle, deg
Δp	Pressure drop, Pa

Abbreviation

CFD	Computational Fluid Dynamics
FEM	Finite Element Method
LES	Large Eddy Simulation
LMTD	Logarithmic Mean Temperature Difference
MAD	Mean Absolute Deviation
MRD	Mean Relative Deviation
NTU	Number of Transfer Units
SST	Shear Stress Transport

Subscripts

ent	Entrance
fd	Fully developed
i	Inlet
m	Mean

o	Outlet
v	Vapor
w	Wall

References

1. Ploug, O.; Vestergaard, B. New microchannel profile for evaporators and for refrigeration condensers. In Proceedings of the 4th International Congress on Aluminium Heat Exchanger Technologies for HVAC&R, Düsseldorf, Germany, 10–11 June 2015.

2. Atkinson, K.N.; Drakulic, R.; Heikal, M.R.; Cowell, T.A. Two- and three-dimensional numerical models of flow and heat transfer over louvred fin arrays in compact heat exchangers. *Int. J. Heat Mass Transf.* **1998**, *41*, 4063–4080.

3. Perrotin, T.; Clodic, D. Thermal-hydraulic CFD study in louvered fin-and-flat-tube heat exchangers. *Int. J. Refrig.* **2004**, *27*, 422–432.

4. Qian, Z.; Wang, Q.; Cheng, J.; Deng, J. Simulation investigation on inlet velocity profile and configuration parameters of louver fin. *Appl. Therm. Eng.* **2018**, *138*, 173–182.

5. Sarpotdar, S.; Nasuta, D.; Aute, V.; Systems, O.; Road, V.M.; Park, C. CFD Based Comparison of Slit Fin and Louver Fin Performance for Small Diameter (3 mm to 5 mm) Heat Exchangers. *Int. Compress. Eng. Refrig. Air Cond.* **2016**, *1988*, 1–10.

6. Jiang, Q.; Zhuang, M.; Zhu, Z.; Shen, J. Thermal hydraulic characteristics of cryogenic offset-strip fin heat exchangers. *Appl. Therm. Eng.* **2019**, *150*, 88–98.

7. Martinez, E.; Vicente, W.; Salinas-Vazquez, M.; Carvajal, I.; Alvarez, M. Numerical simulation of turbulent air flow on a single isolated finned tube module with periodic boundary conditions. *Int. J. Therm. Sci.* **2015**, *92*, 58–71.

8. Peng, H.; Ling, X.; Li, J. Performance investigation of an innovative offset strip fin arrays in compact heat exchangers. *Energy Convers. Manag.* **2014**, *80*, 287–297.

9. Bhuiyan, A.A.; Amin, M.R.; Naser, J.; Islam, A.K.M. Effects of geometric parameters for wavy finned-tube heat exchanger in turbulent flow: A CFD modeling. *Front. Heat Mass Transf.* **2015**, *6*, 1–11.

10. Ismail, L.S.; Velraj, R. Studies on fanning friction (f) and colburn (j) factors of offset and wavy fins compact plate fin heat exchanger-a CFD approach. *Numer. Heat Transf. Part A Appl.* **2009**, *56*, 987–1005.

11. Damavandi, M.D.; Forouzanmehr, M.; Safikhani, H. Modeling and Pareto based multi-objective optimization of wavy fin-and-elliptical tube heat exchangers using CFD and NSGA-II algorithm. *Appl. Therm. Eng.* **2017**, *111*, 325–339.

12. Cléirigh, C.T.Ó.; Smith, W.J. Can CFD accurately predict the heat-transfer and pressure-drop performance of finned-tube bundles? *Appl. Therm. Eng.* **2014**, *73*, 681–690.

13. Lindqvist, K.; Næss, E. A validated CFD model of plain and serrated fin-tube bundles. *Appl. Therm. Eng.* **2018**, *143*, 72–79.

14. Kemerli, U.; Kahveci, K. Numerical Investigation of Air-Side Heat Transfer and Fluid Flow in a Microchannel Heat Exchanger. In Proceedings of the 2nd World Congress on Mechanical, Chemical, and Material Engineering (MCM'16), Budapest, Hungary 22–23 August 2016.

15. Kumar, A.; Joshi, J.B.; Nayak, A.K.; Vijayan, P.K. 3D CFD simulations of air cooled condenser-III: Thermal-hydraulic characteristics and design optimization under forced convection conditions. *Int. J. Heat Mass Transf.* **2016**, *93*, 1227–1247.

16. Chennu, R.; Paturu, P. Development of heat transfer coefficient and friction factor correlations for offset fins using CFD. *Int. J. Numer. Methods Heat Fluid Flow* **2011**, *21*, 935–951.

17. Bacellar, D.; Aute, V.; Huang, Z.; Radermacher, R. Airside friction and heat transfer characteristics for staggered tube bundle in crossflow configuration with diameters from 0.5 mm to 2.0 mm. *Int. J. Heat Mass Transf.* **2016**, *98*, 448–454.

18. Deng, J. Improved correlations of the thermal-hydraulic performance of large size multi-louvered fin arrays for condensers of high power electronic component cooling by numerical simulation. *Energy Convers. Manag.* **2017**, *153*, 504–514.

19. Sadeghianjahromi, A.; Kheradmand, S.; Nemati, H. Developed correlations for heat transfer and flow friction characteristics of louvered finned tube heat exchangers. *Int. J. Therm. Sci.* **2018**, *129*, 135–144.

20. Patankar, S.V.; Liu, C.H.; Sparrow, E.M. Fully Developed Flow and Heat Transfer in Ducts Having Streamwise-Periodic Variations of Cross-Sectional Area. *Trans. ASME. Ser. C, J. Heat Transf.* **1977**, *99*, 180.

21. Martinez-Espinosa, E.; Vicente, W.; Salinas-Vazquez, M.; Carvajal-Mariscal, I. Numerical Analysis of Turbulent Flow in a Small Helically Segmented Finned Tube Bank. *Heat Transf. Eng.* **2017**, *38*, 47–62.

22. Awais, M.; Bhuiyan, A.A. Heat and mass transfer for compact heat exchanger (CHXs) design: A state-of-the-art review. *Int. J. Heat Mass Transf.* **2018**, *127*, 359–380.

23. Qasem, N.A.A.; Zubair, S.M. Compact and microchannel heat exchangers: A comprehensive review of air-side friction factor and heat transfer correlations. *Energy Convers. Manag.* **2018**, *173*, 555–601.

24. Kristófersson, J.; Vestergaard, N.P.; Skovrup, M.; Reinholdt, L. Ammonia charge reduction potential in recirculating systems—Calculations. In Proceedings of the IIR Ammonia Refrigeration Conference, Ohrid, Macedonia, 11–13 May 2017; pp. 80–87.

25. Kristófersson, J.; Vestergaard, N.P.; Skovrup, M.; Reinholdt, L. Ammonia charge reduction potential in recirculating systems—System benefits. In Proceedings of the IIR Ammonia Refrigeration Conference, Ohrid, Macedonia, 11–13 May 2017; pp. 72–79.

26. Lotfi, B.; Sundén, B. Development of new finned tube heat exchanger: Innovative tube-bank design and thermohydraulic performance. *Heat Transf. Eng.* **2019**, *7632*, 1–27.

27. Sahiti, N.; Lemouedda, A.; Stojkovic, D.; Durst, F.; Franz, E. Performance comparison of pin fin in-duct flow arrays with various pin cross-sections. *Appl. Therm. Eng.* **2006**, *26*, 1176–1192.

28. Menter, F.R. Two-equation eddy-viscosity turbulence models for engineering applications. *AIAA J.* **1994**, *32*, 1598–1605.

29. Kim, M.S.; Lee, J.; Yook, S.J.; Lee, K.S. Correlations and optimization of a heat exchanger with offset-strip fins. *Int. J. Heat Mass Transf.* **2011**, *54*, 2073–2079.

30. Chimres, N.; Wang, C.C.; Wongwises, S. Optimal design of the semi-dimple vortex generator in the fin and tube heat exchanger. *Int. J. Heat Mass Transf.* **2018**, *120*, 1173–1186.

31. Chapter 4: Turbulence, 4.16 Near-Wall Treatments for Wall-bounded Turbulent Flows, 4.16.1. In *ANSYS Fluent 19.1 User's Guide*, ANSYS Inc.: Canonsburg, PA, USA, 2019.

32. Shah, R.K.; Sekulic, D.P. *Fundamentals of Heat Exchanger Design*; John Wiley & Sons: Hoboken, NJ, USA, 2003.

33. Webb, R.L.; Kim, N. *Principles of Enhanced Heat Transfer*, 2nd ed.; CRC Press: New York, NY, USA, 2005.

34. Kaminski, U.; Grob, S. Luftseitiger Wärmeübergang und Druckverlust in Lamellenrohr-Wärmeübertragern. *Ki Luft Kaeltetechnik* **2000**, *36*, 13–18.

35. Fraß, K.P.F.; Hofmann, R. *Principles of Finned-Tube Heat Exchanger Design for Enhanced Heat Transfer*, 2nd ed.; WSEAS Press: 2015. Available online: http://www.wseas.org/wseas/cms.action?id=9512 (accessed on 15 September 2019).

36. Shah, R.K.; London, A.L. *Laminar Flow Forced Convection in Ducts*; Academic Press: New York, NY, USA, 1978.